New insight into the Auger decay process in O_2: the coincidence perspective

Tiberiu Arion[1,2], Ralph Püttner[3], Cosmin Lupulescu[4], Ruslan Ovsyannikov[5], Marko Förstel[1], Gunnar Öhrwall[6], Andreas Lindblad[7], Kiyoshi Ueda[8], Svante Svensson[7], Alex M. Bradshaw[1,9], Wolfgang Eberhardt[4,10] and Uwe Hergenhahn[11]

[1]Max-Planck-Institut für Plasmaphysik, EURATOM Association, Boltzmannstr. 2, 85748 Garching, Germany

[2]Institut für Experimentalphysik, Universität Hamburg, Luruper Chaussee 149, 22761 Hamburg, Germany

[3]Institut für Experimentalphysik, Freie Universität Berlin, Arnimallee 14, 14195 Berlin, Germany

[4]Technische Universität Berlin, Institut für Optik und atomare Physik, Hardenbergstr. 36, 10623 Berlin, Germany

[5]Helmholtz-Zentrum Berlin, Albert-Einstein-Str. 15, 12489 Berlin, Germany

[6]MAX-lab, Lund University, P.O. Box 118, SE-22100 Lund, Sweden

[7]Uppsala University, Department of Physics and Astronomy, Box 516, SE-751 20 Uppsala, Sweden

[8]Institute of Multidisciplinary Research for Advanced Materials, Tohoku University, Sendai 980-8577, Japan

[9]Fritz-Haber-Institut der Max-Planck-Gesellschaft, Faradayweg 4-6, 14195 Berlin, Germany

[10]Center for Free-Electron Laser Science, Notkestrasse 85, 22607 Hamburg, Germany

[11]Max-Planck-Institut für Plasmaphysik, EURATOM Association, Teilinstitut Greifswald, Wendelsteinstr. 1, 17491 Greifswald, Germany

Dedicated to Professor Darrah Thomas on the occasion of his 80th birthday

Abstract

Photoelectron-Auger electron coincidence spectroscopy is a powerful tool for the investigation of Auger decay processes with different core-ionized intermediate states. In this paper we describe an investigation into the Auger decay of the O_2 molecule, with the purpose of bringing new insight into the dynamics of the core hole decay mechanism. Using a novel experimental approach to measuring such coincidence spectra we report the highest resolution Auger spectrum of O_2 recorded hitherto. In our approach, we have combined the advantages of these coincidence spectra with the high resolution and excellent signal-to-noise ratios of non-coincident Auger spectra and a state-of-the-art fit analysis. In this way we have derived information about the potential energy curves of the final states W $^3\Delta_u$, B $^3\Pi_g$, and B' $^3\Sigma_u^-$ and concluded that the corresponding Auger transitions are formed to a large part by strongly overlapping vibrational progressions. The present findings are compared to earlier results reported in the literature confirming some theoretical predictions.

PACS

07.81.+a, 07.85.Qe, 29.30.Dn, 32.80.Hd, 33.80.Eh

1. Introduction

Electron spectroscopy has emerged in the last few decades from fundamental science into a useful analytical tool for materials research. If material (atom, molecule or condensed matter) is ionized with a photon of sufficiently high energy, more than one electron can be emitted in a single ionization event. The requirement for spectroscopic detection of two such electrons in *coincidence* is motivated by the need to learn more about electron correlation as well as to gain a better understanding of conventional (non-coincident) electron spectra. One example for which numerous electron-electron coincidence studies have been performed is inner shell photoionization followed by the emission of an Auger electron. After the first successful experimental study of this problem by T. Darrah Thomas and co-workers [1] other authors followed, both in the solid state [2][3][4] and the atomic and molecular physics communities [5][6][7][8][9][10][11][12][13][14][15][16]. A somewhat more detailed overview has been given in Ref. [17].

For molecular Auger decay in particular, photoelectron-Auger electron coincidence spectroscopy offers the possibility of disentangling the Auger spectrum into contributions from individual intermediate (singly charged) states, which otherwise overlap in the same energy region. These state-selected Auger spectra also allow for a better separation of the final (dicationic) states, which are hard to access by other (conventional) spectroscopic techniques. A decisive factor for the appearance of molecular Auger spectra is the nature of the potential curves, whether they are bound, metastable or repulsive. For the inner shell-ionized states both bound and repulsive curves are possible. One would naively expect the final state always to be repulsive, but in fact a number of metastable dicationic states of small molecules have been found [18]. These can even support vibrational levels (see below). For transitions from bound to metastable states the vibrational levels of both states can sometimes be inferred from a meticulous analysis of very high quality non-coincident photoelectron and Auger electron spectra [19]. As soon as the transitions involve a repulsive potential curve, however, there is no alternative but to disentangle the various contributions in an electron-electron coincidence experiment [20].

In this paper we present a novel apparatus for recording electron pairs in coincidence. A defining feature of our apparatus is the very high energy resolution, which is even maintained for high kinetic energy electrons (e.g. an Auger electron). We have reconciled the contradictory requirements of large solid angle of detection, multiplex recording of the electrons and strong retardation of the fast electrons by combining a large hemispherical electron analyzer (VG Scienta R4000) with a novel electron time-of-flight spectrometer (VG Scienta ArTOF 10k) [21]. The latter instrument allows electrons to be collected from within a cone of ±15° opening angle (depending on the settings of the analyzer) using an electrostatic lens. This optics can be used to produce an angle-to-point mapping of the interaction point onto a spatially resolving detector. The pathlength difference of trajectories pertaining to equal energy electrons is accounted for, and thus the energy resolution of the instrument is decisively better than that of conventional time-of-flight analyzers [17]. Interestingly, in the coincident spectrum the reference time for the ArTOF spectrum can be derived from the electron arrival time in the other spectrometer, so that operation of the ArTOF with a quasi-continuous light source, such as synchrotron radiation in multi-bunch mode, becomes possible.

Although it has only been applied so far to molecules in the gas phase, our detection scheme is general and can find applications in the observation of electron pairs from the solid state, e.g. to elucidate the decay of quasi-particles excited by photoionization [22], or more generally to study electron correlation in matter [23].

As an example of data recorded with the new instrument we present the Auger spectrum of molecular oxygen (O_2) separated into components from the O $1s^{-1}$ ($^2\Sigma^-$) and the O $1s^{-1}$ ($^4\Sigma^-$) inner shell ionized states. We also present a conventional (non-coincident) K-VV spectrum measured with a higher energy resolution than those reported earlier. By using all this information in a fit analysis,

we are able to reliably assign the features in the non-coincident spectrum. For some of the Auger lines we find evidence for a vibrational structure, that is, for dicationic states which are populated in a metastable region of their potential curve. We compare our results from the fit analysis with recent theoretical calculations of high quality [24].

The inner shell photoelectron spectrum of O_2 has been reported several times, most recently in Ref. [25]. As already mentioned above, it consists of two 1s main lines, which form due to the exchange coupling of the open valence shell (triplet spin) to the core hole. The core-ionized state can thus have quartet or doublet spin, resulting in binding energies of 543.39(5) and 544.43(5) eV, respectively [25]. Besides this exchange splitting, each of the main lines exhibits a vibrational structure, which in particular in the $^2\Sigma^-$ line shows up as a clear asymmetry of the peak profile [25] [26]; Due to the lifetime broadening of 140(5) meV which is identical to the vibrational splitting of 140 meV for the $^2\Sigma^-$ line state [25], it has not been possible to observe the individual vibrational peaks so far. As O_2 is a homonuclear diatomic molecule, its core levels may also show a *gerade/ungerade* splitting, akin to N_2 [27] and C_2H_2 [28][29]. For O_2 this splitting has been calculated as 26 meV [30]. More recently, in Ref. [25], values of 50 and 7 meV were given for the $^4\Sigma^-$ and the $^2\Sigma^-$ states, respectively. These values were not in contradiction with the experimental data presented in the same paper. Our results give evidence for an even larger *g/u* splitting in the $^4\Sigma^-$ state and are discussed below.

Early studies on the normal Auger spectrum of O2 were performed by Siegbahn [31] and by Moddeman et al. [32]. Later on, Larson et al. [33], combined experiment and theory to give a detailed discussion of the Auger spectrum of oxygen. Many different authors conducted additional theoretical work. For an overview of this theoretical work see Bao et al. [24], who performed extended calculations, including potential curves for all dicationic final states. Most recently, a part of the Auger spectrum was recorded in coincidence with the pertaining photoelectrons using the predecessor of the instrument described in this paper [17].

The dicationic states of oxygen can also be probed by other methods, most notably single photon photo double ionization. Results from a study using this method have been published earlier [34][35]. These authors stress the important role played by sequential processes (single photoionization into an excited state, followed by dissociation and atomic autoionization) in valence double ionization of O_2. In our study, we believe that the nuclear dynamics in the intermediate state is only important to the extent that is taken into account by lifetime vibrational interference. The energies of the lowest doubly ionized states of O_2 have been determined earlier by coincidence spectroscopy of threshold electrons [36].

2. Experimental Set-up

The experimental apparatus is shown schematically in Figure 1. It consists of a vacuum chamber, fitted with two high-resolution electron spectrometers, situated in the horizontal plane. The analyzers are placed at 90° to each other, and at 45° with respect to the direction of the synchrotron radiation [37]. The apparatus can be used for a variety of investigations, ranging from conventional Auger spectroscopy, XPS or angular-resolved photoemission (ARPES) on condensed matter samples [38]**,** to spectroscopic investigation on gaseous probes.

For recording the fast Auger electrons, we have chosen to use a hemispherical electron energy analyzer of the Scienta R4000 (VG Scienta AB, Uppsala, Sweden) type (central radius 200 mm), which is specified to deliver a maximum energy resolution of 1.7 meV, provided that a small entrance slit in the hemisphere and a small pass energy are used. Conventional (non-coincident) electron spectra with this analyzer are recorded by sweeping the lens voltages, and detecting the ensuing electron spectra by reading out the signal of a microchannel plate detector via a CCD camera. We have instead used this analyzer with a delay-line anode to accomplish a fast, position-resolved detection of single electrons, which is needed in a coincidence experiment. At fixed settings of the analyzer voltages, we can thus record electrons within an energy interval with a width of about 10 % of the pass energy. In the experiment shown here, we have chosen to

investigate the Auger final states of the O_2 molecule over a rather broad energy range of about 15 eV. In order to acquire all features, we have used a pass energy setting of 200 eV.

The photoelectrons were recorded using a new generation, very high-resolution time-of-flight electron spectrometer, of the Scienta ArTOF 10k (VG Scienta AB, Uppsala, Sweden) type [21]. Basically, this analyzer consists of an electrostatic lens system and a fast, spatially resolving electron detector. By virtue of the electron lens, the spectrometer can be operated such that it delivers an angle-to-point mapping from the source region to the detector. In other words, the hit position of each electron on the spatially resolving detector is a measure of its take-off angle from the sample, or source region measured relative to the spectrometer axis. Referring to ray-tracing calculations, from the time-of-flight (t) and the distance (r) of the impact position to the detector centre it is possible to calculate back on the original electron kinetic energy E(r,t) and the emission angle. Because the spectrometer does not have an entrance aperture, all electrons emitted within a cone of maximum 15° opening angle (depending on the lens voltages) are detected. While this opens new horizons for ARPES [38][39][40][41], another effect of this arrangement is to conveniently sort electron trajectories by their length, since the main factor on which the length depends is just the entrance angle relative to the spectrometer axis. As the path length differences of electrons with equal energy are a major source of energy broadening in conventional linear time-of-flight analyzers [42], it follows that the ArTOF is not only efficient but also can have an excellent energy resolution, up to 160 μeV according to the specifications.

For experiments on molecular samples, a gas cell was constructed, which reduces the size of the interaction region seen by the two spectrometers and thus helps to improve the alignment of the experimental setup for the optimum coincidence signal. A source region with sub-mm dimensions is also a prerequisite for a successful reconstruction of the ArTOF trajectories. For the linear spectrometer, the opening of the gas cell is round, with a diameter of 1 mm. For the hemispherical analyzer, the opening of the gas cell does not artificially limit the geometry of the interaction region seen by spectrometer, when the set-up is properly aligned.

Electron spectroscopy with the ArTOF system usually requires a pulsed excitation source. Our experiments were performed at the U49/2-PGM1 branch of the BESSY II synchrotron radiation source, which is run in two different modes: the single bunch mode and the hybrid (multi-bunch) mode. In the single bunch mode, only one electron packet is injected into the storage ring. The resulting 800 ns period of photon bunches is sufficient for disentangling the single bunches in both spectrometers. The flight time in the ArTOF was of the order of 700 ns for electron kinetic energies around 36 eV, as used in our experiment. However, since the combined solid angle of detection of our spectrometers is still limited, the time needed to record a coincidence spectrum with sufficient statistics and an acceptable ratio of true-to-random coincidences would be impracticably long. Therefore we have chosen to perform the experiment in the hybrid mode, where a 350 electron packets of 20-30 ps length, 2 ns apart are injected into the storage ring, followed by a dark gap of 100 ns, in the middle of which a single electron bunch (hybrid peak) is injected [43]. As the spectra produced by the 350 bunches are so close to each other, they cannot be disentangled, giving rise to a background, on top of which one can distinguish the time of flight spectrum produced by the hybrid bunch [17].

In order to use the ArTOF in hybrid mode, an alternative start signal for the time-of-flight measurement must be provided. In our experiment, we have derived this signal from the arrival time of the Auger electron in the hemispherical analyzer. As the transit time of electrons in this device can be taken as a constant in a first approximation, we can determine the photoelectron spectrum from the ArTOF data for all coincident events. A thorough discussion of the timing properties of hemispherical analyzers and of the practical implementation of this timing scheme has been given [17][44][45].

The energy resolution in the experiment described here was set sufficiently good to separate the two multiplet levels of the O 1s core ionized state. From a lineshape analysis of our measured spectra, we have estimated it as 500 meV for the coincidently detected photoelectrons, including beamline and all analyzer contributions. Some more words about the potential energy resolution of

this set-up are in order. The contributions of the beamline and of the hemispherical analyzer to the energy broadening can be characterized by well-known methods, and can both be well below 100 meV with present technology. The main factors contributing to the energy resolution of the ArTOF system as a *non-coincident* electron analyzer have also been discussed [46]. We note that in our (gas phase) application the extension of the interaction region both along and perpendicular to the spectrometer axis will make notable contributions. Estimates show that nevertheless an energy resolution better than 50 meV can be expected. These are based on a proper account of the E(r,t) function of the ArTOF, which has not been applied to the current data set.

The most important single factor contributing to the energy resolution for *coincident* photoelectrons will be the temporal broadening added by the hemispherical analyzer. Generally, this factor becomes larger when the angle interval in which electrons may enter the hemispheres is increased, or when the pass energy is decreased. A trade-off between true coincidence count rate, desired Auger electron energy resolution, and photoelectron energy resolution therefore must be chosen. In an unpublished coincidence experiment we have recorded the photoelectrons pertaining to a molecular Auger line at 9.2 eV kinetic energy with an analyzer energy resolution of 44(5) and 115(10) meV for non-coincident and coincident events, resp. The non-coincident energy resolution has been determined from the hybrid bunch signal. More details will be given [37].

The spectra are calibrated using the binding energy of 544.43(5) eV for the O $1s^{-1}$ ($^2\Sigma^-$) core level [25] as well as a double-ionization potential of 43.550(5) eV for the dicationic B $^3\Pi_g$ state [36]; the energy position of the v' = 0 level of this state is determined within the present data analysis with an accuracy of 10 meV, see below. In this way an accuracy of 65 meV for the kinetic energy axis of the Auger spectra and an accuracy of 50 meV for the double ionization potential of the final-state energy spectrum are achieved.

3. Results and discussion: high resolution photoelectron-Auger electron coincidence spectra of molecular oxygen

3.1 Experimental data

The recent investigations of Bao and co-workers on the O_2 molecule focus on separating the Auger spectra corresponding to the individual cationic states [24]. As an experimental starting point, they use a high resolution Auger spectrum of O_2 recorded by conventional Auger spectroscopy.

We have re-measured this Auger spectrum with the hemispherical analyzer of our set-up using a photon energy of 573.1 eV (Figure 2a). The energy resolution is superior to that of earlier published spectra [33], while its shape and the kinetic energies of the main features are generally in good agreement with the latter. In the course of performing a Franck-Condon data analysis (see below) we have nevertheless noted the occurrence of very small inhomogeneities at kinetic energies between 499 and 500 eV (see vertical arrows in the inset of Fig. 2). These features seem neither to be present in earlier published spectra, nor in unpublished spectra recorded earlier by two of the authors of the present paper. We have therefore compared the spectrum of Fig. 2a with another, published high-resolution conventional Auger spectrum of O_2 (Fig. 2b), which is less structured in the highlighted region. The latter spectrum was recorded at the SU27 beamline of SPring8 with an r = 200 mm hemispherical electron analyzer under comparable settings, but at a different photon energy, namely 650 eV, and at a total resolution of 80 meV [49]. Statistical fluctuations of the count rates as the origin of the differences can be excluded since in the inset the data points are already larger than the error bars. A resonant process, such as autoionization of neutral doubly excited states, might be a natural explanation for these small differences, but without further data from a dedicated experiment we cannot positively confirm this. An assignment to doubly excited states would be in line with optical luminescence excitation spectra of molecular oxygen in the energy region above the O 1s ionization threshold, which show a broad peak around 575 eV [50], i.e. very close to the excitation energy of 573.1 eV used for the spectrum shown in Fig. 2a. Some years after

the discovery of luminescence excitation, the spectra were explained by Mahalingam and Hanson [51] in terms of decay of the inner-valence two-hole and three-hole, one-electron states produced by Auger decay of molecular oxygen. This observation is also in line with the assumption of neutral doubly excited states in the energy region around 575 eV. Sample impurities are another conceivable explanation for the differences shown.
In the used geometry the presence of non-dipole effects in the PES cannot be excluded [52]. Since it is commonly assumed that the matrix elements for the entire process of ionization and Auger decay can be written as a product of the matrix elements of the individual steps [53] the Auger spectrum can only be influenced by these non-dipole effects in respect to its angular distribution function. We also note that most recent experiments found only small non-dipole effects in molecular core level photoemission [54].

The Franck-Condon fit analysis, see below, was performed using both spectra presented in Fig. 2. Although the differences between these two spectra around 499 eV are evidently very small, we want to point out that a consistent fit result, i.e. a good agreement with the spectra in combination with reasonable results for the fit parameters, was obtained only for the spectrum recorded at SPring 8. This clearly demonstrates the high sensitivity of the Franck-Condon analysis to spectral features that are not correctly taken into account in the fit analysis. We have thus used the SPring8 spectrum (Fig. 2b) as the reference spectrum in the fit analysis described below. Figure 3 shows, in the center panel, the photoelectron-Auger electron coincidence spectrum of O_2, as recorded at a photon energy of 573.1 eV. The kinetic energy of the Auger electrons is displayed on the vertical axis, on the left hand side, while the energy of the photoelectrons is shown on the horizontal axis. The regions of stronger intensity in the color-coded map indicate the events where both electrons, emitted in the photoionization and the Auger decay process, have been detected by the two detectors.

By projecting the coincidence spectrum on the horizontal axis, one obtains the photoelectron energy spectrum, as shown in the upper panel. One can easily distinguish the $^2\Sigma^-$ and $^4\Sigma^-$ states of the cation, which are 1.06 eV apart [25].

In the right-hand panel of Figure 3 we show the coincident Auger spectrum of the O_2 molecule, as obtained by summing the entire coincidence map along the horizontal axis. If one chooses to select from the coincidence spectrum only the regions indicated by the red and black rectangles in the central panel, one obtains the Auger spectra pertaining to the individual intermediate states of the singly charged cation. The one-dimensional Auger energy spectra obtained from this selection procedure are presented in Figure 4, as well as in more detail in Figs. 6 and 8; the latter two figures contain also the results of the fits for the individual curves (see below).

Figure 4 shows the high-resolution normal Auger spectrum of O_2 measured at Spring8 together with the Auger spectra due to $^2\Sigma^-$ and the $^4\Sigma^-$ core ionization. The state-resolved Auger spectra resulting from O $1s^{-1}$ ($^2\Sigma^-$) and O $1s^{-1}$ ($^4\Sigma^-$) core ionization have been assembled from two data sets, namely one high-resolution spectrum ranging from 497 eV to 503 eV and one spectrum with lower resolution for kinetic energies above and below this range. While the latter partial Auger spectra are a result of this work, the former are part of an earlier data set recorded by some of the authors [17]. The high resolution data set was introduced to particularly address the W $^3\Delta_u$, B $^3\Pi_g$, and B' $^3\Sigma_u^-$ final states in the kinetic energy range from 498 to 503 eV, since from earlier work these are known to have a clear minimum in their potential energy curve, thus hosting vibrational progressions [48][55].

3.2 Data analysis and results

In this section we will describe the data analysis and discuss the results. Qualitatively, the Auger spectrum presented in Fig. 2 can be separated in three regions. The first region spans the kinetic energy region above 503 eV and consists of satellite Auger transitions; they will be discussed towards the end of this section. The energy interval between 498 eV and 503 eV of the spectrum is dominated by Auger transitions to metastable final states, as discussed above. By

contrast, no metastable final states are either known or expected in the third region below 498 eV, so that the fit approaches for the latter two regions are different. After summarizing information from literature about the O $1s^{-1}$ photoelectron spectrum we will discuss the resulting consequences for the presence of vibrational lifetime interference in the Auger spectrum. After this, we will discuss the Auger transitions to the metastable final states (region 2 ranging from 498 eV to 503 eV) followed by Auger transitions to the dissociative final states (region 3 below 498 eV).

The O $1s^{-1}$ photoelectron spectrum [25] exhibits strongly overlapping vibrational levels since the vibrational energies and the lifetime broadening are in the same order of magnitude. From this observation the presence of lifetime interference contributions in the Auger spectrum can be anticipated; and consequently vibrational lifetime interference was taken into account in the simulations of Bao et al. [24]. Contrary to this, electronic lifetime interference can safely be neglected since the two core hole states O $1s^{-1}$ ($^2\Sigma^-$) and O $1s^{-1}$ ($^4\Sigma^-$) are well separated in energy. Sorensen et al. [25] also reported a splitting of 50 meV into a *gerade* and an *ungerade* component for the O $1s^{-1}$ ($^4\Sigma^-$) core-hole state. However, as already discussed for the case of N_2, the *gerade/ungerade* splitting of a core hole does not lead to interference contributions. This is due to the fact that a population of a given dicationic final state via the *gerade* or the *ungerade* core hole state requires different symmetries for both, the photoelectron and the Auger electron such that the total final state consisting of the dicationic final state, the photoelectron, and the Auger electron is different [56].

3.2.1 The O $1s^{-1}$ → W $^3\Delta_u$, B $^3\Pi_g$, and B' $^3\Sigma_u^-$ Auger transitions

As discussed above, using different techniques experimentally resolved vibrational levels are reported for the final states W $^3\Delta_u$, B $^3\Pi_g$, and B' $^3\Sigma_u^-$ [48][55]. By contrast, no obvious vibrational structures are observable in the Auger spectrum. There can be several reasons for this: Firstly, the Auger transitions may populate the dissociative part of the potential energy curves. Secondly, the observed vibrational splittings for the final states W $^3\Delta_u$, B $^3\Pi_g$, and B' $^3\Sigma_u^-$ are 104, 176 and 131 meV [48], respectively. These values are of the same order of magnitude as the lifetime broadening so that the vibrational levels are partially masked and difficult to observe. The visibility of vibrational structures might also be reduced by vibrational lifetime interference contributions of overlapping Auger transitions. In the case of the O $1s^{-1}$ ($^4\Sigma^-$) core hole state the reported splitting of 50 meV into a *gerade* and an *ungerade* component [25] will further decrease the visibility of the expected vibrational structure; such a partial masking has been observed for N_2 [56], which also exhibits a *gerade/ungerade* splitting.

In order to clarify whether vibrational structures are expected in the Auger spectrum, the energy region from 498 eV to 503 eV has been described in a fit analysis by assuming the presence of vibrational sub-states. This data analysis is based on the Kramers-Heisenberg formula and described in detail in Refs. [19][57]; here we summarize only the major ideas and the differences to the previously used procedures. To calculate the Franck-Condon factors (FCF), we assume Morse potentials for the ground state, the core-ionized states, and the dicationic final states. Besides the energy position for the minimum, a Morse potential is described by three parameters, namely, the vibrational energy $\hbar\omega$, the anharmonicity $x\hbar\omega$, and the equilibrium distance R_e. The values of these parameters for the potential energy curves of the ground state and the core-ionized state can be taken from the literature [25][58]. For the final states the vibrational energies were fixed to the values reported by Ref. [48]. This reference also reports values for the anharmonicities; when these are introduced in our simple approach based on Morse potentials it fails however for computational reasons. Because of this we use values for the anharmonicities which are in line with our computational limits, but are as close as possible to the reported values; the used values are 30% to 50 % lower than those reported by Lundqvist et al. [48]. The energy splitting between the $v''= 0 \rightarrow v' = 0$ Auger transitions starting from the O $1s^{-1}$ ($^2\Sigma^-$) and O $1s^{-1}$ ($^4\Sigma^-$) core hole as well as those from the *gerade* and the *ungerade* component of the O $1s^{-1}$ ($^4\Sigma^-$) core hole are taken from the reported photoelectron spectrum [25]. Furthermore, because for N_2 the Auger intensities for a *gerade* and an

ungerade core hole are observed to be significantly different [56], we also allowed different intensities for the *gerade* and the *ungerade* component of the O $1s^{-1}$ ($^4\Sigma^-$) core hole. In summary, the energy positions and equilibrium distances of the dicationic final states as well as the intensities of the Auger transitions (with the exception to the O $1s^{-1}$ ($^2\Sigma^-$) → B' $^3\Sigma_u^-$ transition, see below) were used as free parameters while the vibrational energies and anharmonicities were fixed.

In the analysis of the energy region of the Auger transitions to the final states W $^3\Delta_u$, B $^3\Pi_g$, and B' $^3\Sigma_u^-$ post-collision interaction (PCI) is taken into account. The direct terms of the Kramers-Heisenberg formula are described using the PCI lineshapes given by Armen et al. [59] while the less important cross terms (lifetime interference terms) are modeled with the lineshapes given by the Kramers-Heisenberg formula by including an average energy shift to approximate the photoelectron relaxation. These lineshapes were convoluted with a Gaussian of 80 meV full-width-half-maximum (FWHM) to account for the experimental resolution.

The high-resolution conventional Auger spectrum measured at Spring8 (as described above) including the fit result is shown in Figure 5. For comparison, Figure 6 shows the same spectrum together with sub-spectra derived from the fit analysis that display the contributions of the O $1s^{-1}$ ($^2\Sigma^-$) and the O $1s^{-1}$ ($^4\Sigma^-$) Auger transitions as well as the corresponding high-resolution Auger spectra obtained from the coincidence measurements. As already mentioned above the intensity for the O $1s^{-1}$ ($^2\Sigma^-$) → B' $^3\Sigma_u^-$ Auger transition is a fixed parameter in order to better match the Auger spectra obtained from the coincidence measurements (see Fig. 6c). Treating the O $1s^{-1}$ ($^2\Sigma^-$) → B' $^3\Sigma_u^-$ Auger intensity as a free parameter results in values for the O $1s^{-1}$ ($^2\Sigma^-$) → B $^3\Pi_g$ and O $1s^{-1}$ ($^2\Sigma^-$) → B' $^3\Sigma_u^-$ Auger transitions, which are not consistent with the coincidence measurements.

The fit result shown agrees very well with the high-resolution normal Auger spectra and the Auger spectra obtained from the coincidence measurements. The vertical-bar diagrams in the middle of Figure 5 indicate the fit results for the energy positions of the v'' = 0 → v' = 0 Auger transitions as well as the relative Auger intensities. The energy splitting obtained between the v'' = 0 → v' = 0 transitions of the B' $^3\Sigma_u^-$ Auger transition and the B $^3\Pi_g$ (W $^3\Delta_u$) Auger transition amounts to 200 meV (1140 meV). The splitting between the B' $^3\Sigma_u^-$ and the B $^3\Pi_g$ Auger transition agrees with the value of 204 meV derived from Doppler-free kinetic energy release spectroscopy [55] with vibrational resolution. Contrary to this, the present energy splitting between the B' $^3\Sigma_u^-$ and the W $^3\Delta_u$ Auger transition is 140 meV larger than the values obtained by Lundqvist et al [48]. However, even in the high-resolution kinetic energy release spectra of Ref. [48], only three vibrational sub-states could be observed for the dicationic final state W $^3\Delta_u$, suggesting a very shallow minimum in the corresponding potential energy curve. We conclude that the Morse potential used to describe the final states in case of the state W $^3\Delta_u$ differs considerably from the true potential and does not allow highly accurate values for the energy position and the equilibrium distance to be derived, see below.

The intensities obtained for all three Auger transitions show, within the error bars, no significant dependence on the O $1s^{-1}$ core hole; this observation is in full agreement with the Auger intensities calculated by Bao et al. [24]. Furthermore, we obtained intensity ratios of 1:1.4 and 1:3.5 for the O $1s^{-1}$ → B $^3\Pi_g$ to O $1s^{-1}$ → B' $^3\Sigma_u$ and the O $1s^{-1}$ → B $^3\Pi_g$ to O $1s^{-1}$ → W $^3\Delta_u$ Auger transitions. These values are also in good agreement with the ratios of 1:1.2 and 1:3.3, respectively, obtained from the calculations of Bao et al. [24].

From our fit we obtained equilibrium distances of 1.37(2) Å, 1.18(2) Å, and 1.35(1) Å for the dicationic final states W $^3\Delta_u$, B $^3\Pi_g$, and B' $^3\Sigma_u^-$, respectively. These values agree reasonably well with the theoretical values of 1.38 Å, 1.21 Å, and 1.35 Å reported by Lundqvist et al. [48] as well as with the 1.37 Å, 1.21 Å, and 1.34 Å reported by Furuhashi et al. [55].

The upper solid-line sub-spectra below the normal Auger spectrum ("total" in Fig. 5) show contributions of the Auger transitions to the individual final states, while the lower solid-line sub-spectra show the lifetime interference contributions. The dashed-line sub-spectra indicate calculated vibrational progressions for which the vibrational lifetime interference contributions were neglected. The profile obtained for the Auger transition to the final state W $^3\Delta_u$ agrees well with that of Bao et al. [24], which was calculated by using the theoretical potential energy curve instead of a

Morse potential. This finding in combination with the good agreement of the experimental and theoretical equilibrium distances confirms that the assumption of the Morse potential in the fit analysis leads to a reasonable description of the spectrum, although deviations of the true potential from the assumed Morse potential are well known to exist. Furthermore, the present study confirms the observation of Bao et al. that vibrational lifetime interference has a significant influence on the lineshapes.

Figs. 5 b to d show the contributions of the fit result that can be assigned to the O $1s^{-1}$ ($^2\Sigma^-$), the O $1s^{-1}$ ($^4\Sigma^-_u$), and the O $1s^{-1}$ ($^4\Sigma^-_g$) core hole, respectively. Interestingly, all these sub-spectra show vibrational structures for the O $1s^{-1} \rightarrow$ B $^3\Pi_g$ and O $1s^{-1} \rightarrow$ B' $^3\Sigma_u^-$ transitions. This holds in particular for the Auger transitions originating from the O $1s^{-1}$ ($^4\Sigma^-$) core level, i.e. the vibrations are masked to a large extent by the *gerade/ungerade* splitting of these core hole states by 50 meV. At this point we would like to emphasize that, according to the present analysis, the sharp peak at 499.7 eV is predominantly due to the O $1s^{-1}$ ($^4\Sigma^-$) v''= 0 $\rightarrow$ B $^3\Pi_g$ v' = 0 transition and its width is due to the *gerade/ungerade* splitting. Improved fit results for this energy region could be obtained by using a *gerade/ungerade* splitting of 75 meV, i.e. a value significantly larger than that reported by Sorensen et al. [25]. Because of the complexity of the present Auger spectrum we interpret this value for the splitting with care, however, conclude that further studies on the O $1s^{-1}$ photoelectron spectrum with improved experimental resolution and signal-to-noise ratio would be an interesting topic.

As mentioned above, the high-resolution $^4\Sigma^-$ and $^2\Sigma^-$ Auger spectra are shown in Figs. 6 b and c, respectively. The upper solid-line sub-spectra in this part of the figure indicate the corresponding contributions of the spectra as obtained from the fit described in Fig. 5. Obviously, the fit result is fully in line with the $^4\Sigma^-$ and $^2\Sigma^-$ Auger spectra obtained from coincidence measurements. As discussed above, the sub-spectra for the O $1s^{-1} \rightarrow$ B $^3\Pi_g$ and O $1s^{-1} \rightarrow$ B' $^3\Sigma_u^-$ Auger transitions indicate weak contributions from the poorly resolved vibrational sub-states. They are more pronounced in the $^2\Sigma^-$ Auger spectrum because the *gerade/ungerade* splitting of 50 meV of the O $1s^{-1}$ ($^4\Sigma^-$) core-hole state leads to an additional masking of the vibrational splittings.

The lower sub-spectra in Figs. 6 b) and c**)** show simulated Auger spectra originating from the O $1s^{-1}$ ($^2\Sigma^-$) v = 0 and O $1s^{-1}$ ($^4\Sigma^-$) v= 0 core levels by assuming a lifetime broadening of 100 meV and no experimental broadening. These spectra exhibit strong vibrational progressions and support the expectation that vibrational progressions are also present in the experimental Auger spectra. Such Auger spectra with a resolution below the lifetime broadening can – in principle – be obtained from high-resolution coincidence spectra measured with a photon bandwidth smaller than the lifetime broadening and with a very good signal-to-noise ratio. Such measurements can be a topic for future studies and would provide detailed information about the potential energy curves involved in the Auger process including accurate values for the *gerade/ungerade* splitting of the O $1s^{-1}$ ($^2\Sigma^-$) core level.

The results of the present fit analysis allow the final-state energy spectra as presented by Ulrich et al. [17] to be readily simulated. These spectra are displayed in Fig. 7 and show for the final states W $^3\Delta_u$, B $^3\Pi_g$, and B' $^3\Sigma_u^-$ the population of the individual vibrational sub-states subsequent to the Auger decays of the core-hole states O $1s^{-1}$ ($^4\Sigma^-$) and O $1s^{-1}$ ($^2\Sigma^-$). This information potentially allows quantitative studies on the decay of the dicationic final states subsequent to the Auger process, e.g. by comparing with kinetic energy release spectra. Such final-state energy spectra are obtained by integrating the events in the coincidence map along diagonals with constant values for $E_{final} = h\nu - E_{photoelectron} - E_{Auger\ electron}$ (see Fig. 3).

From the significant intensity difference in the energy region around 43.7 eV, Ulrich et al. concluded that the B $^3\Pi_g$ state is populated only via the O $1s^{-1}$ ($^4\Sigma^-$) core-hole state, but not via the O $1s^{-1}$ ($^2\Sigma^-$) core-hole state. The upper solid-line sub-spectrum in each part of the spectrum displays the result of the simulation, which obviously describes the experimental results very well. In each case, the three lower sub-spectra indicate the contributions of the individual final states. The significantly different vibrational progressions in the $^4\Sigma^-$ and the $^2\Sigma^-$ spectra are clearly due to the

different equilibrium distances of the core-hole states; this difference is in particular significant for the transitions to the B $^3\Pi_g$ final state. While in an earlier study from a simple comparison of the peak shapes it was suggested that the B $^3\Pi_g$ state is not populated from the $^2\Sigma^-$ core hole [17], our more sophisticated analysis now reveals that in fact such decays take place, but lead to a much less peaked profile than those from the $^4\Sigma^-$ state.

3.2.2 The O $1s^{-1} \rightarrow 1\pi_u^{-2}$, $3\sigma_g^{-1}\,1\pi_u^{-1}$, and $3\sigma_g^{-2}$ Auger transitions

According to the calculations by Bao et al. [24] the dominant contributions to the spectrum in the kinetic energy region below 498 eV are expected to originate from Auger transitions to dissociative final states so that a Franck-Condon approach is not adequate. Instead, a fit procedure using individual lines is applied and the three spectra are fitted simultaneously in order to use the excellent signal-to-noise ratio and the high spectral resolution of the conventional Auger spectrum, as well as the additional information about the core-hole state derived from the coincidence measurements. Since lifetime vibrational interference (see above) and the shape of the potential energy curves can lead to different lineshapes for the Auger transitions, asymmetric Gaussian shapes with individual asymmetry parameter and width are used. In the fit analysis the well-known splitting between the core-hole states O $1s^{-1}$ ($^2\Sigma^-$) and O $1s^{-1}$ ($^4\Sigma^-$) is not applied since the reasons that lead to the asymmetry are also expected to influence the peak positions.

Fig. 8 shows the total normal Auger spectrum as well as the $^2\Sigma^-$ and the $^4\Sigma^-$ Auger spectra. The solid lines through the data points indicate the fit result and the sub-spectra display the contributions of the individual peaks. Peaks present with similar intensities in both the $^2\Sigma^-$ and the $^4\Sigma^-$ Auger spectra are indicated with solid lines, while peaks occurring predominately or solely in the $^4\Sigma^-$ or in the $^2\Sigma^-$ Auger spectra are indicated with dashed and dash-dotted lines, respectively. The peak positions and the assignments are summarized in Table 1.

Most of the observed peaks were already assigned by Bao et al. [24]; these authors denoted the most intense transitions in this energy region originating from the O $1s^{-1}$ ($^4\Sigma^-$) core-hole state by numbers between 4 and 10. The Auger transitions originating from the O $1s^{-1}$ ($^2\Sigma^-$) core-hole state are indicated by an additional prime, i.e. 4’ to 10’. The present data analysis using the $^2\Sigma^-$ and the $^4\Sigma^-$ Auger spectra is fully in line with the assignment given by Bao et al. Consequently, we adopted their labeling and their assignments of the Auger transitions, see Table 1. Note that for some configurations there are different states with the same symmetry. There are e.g. four $^3\Pi_u$ states that belong to the $3\sigma_g^{-1}\,1\pi_u^{-1}$ configuration. This is due to the fact that O_2 in the ground state is an open-shell molecule with 2 electrons in the $1\pi_g$ orbital, which can couple to $^3\Sigma_g^-$, $^1\Delta_g$, or $^1\Sigma_g^+$. A coupling of the holes in the $3\sigma_g$ and the $1\pi_u$ orbital to these states result in four different $^3\Pi_u$ states.

From our fit we obtained for the O $1s^{-1}$ ($^4\Sigma^-$) $\rightarrow$ $3\sigma_g^{-1}\,1\pi_u^{-1}$ ($^3\Pi_u$) Auger transition (also labeled 8) a total width of 330 meV. Considering a lifetime broadening of 140 meV and a *gerade/ungerade* splitting of 50 meV for the O $1s^{-1}$ ($^4\Sigma^-$) core hole, this leads to two explanations for the observed total width. First, the final state could have a very short vibrational progression, i.e. it is metastable with an equilibrium distance close to that of the O $1s^{-1}$ ($^4\Sigma^-$) core-hole state of 1.23 Å. Second, this state could have a dissociative potential energy curve with a flat slope at the internuclear distance of 1.23 Å. Moreover, there might be additional transitions, some of which are labeled a to d, contributing to both the $^2\Sigma^-$ and the $^4\Sigma^-$ Auger spectra. These structures could be due to additional Auger transitions, which originate from both core-hole states. However, an assignment of the transitions based on the calculations of Bao et al. is not possible.

3.2.3 The satellite Auger transitions

Finally we would like to discuss the two weak features observed in the conventional Auger spectra of Fig. 2 at 504.4 eV and 506.4 eV. These structures have been observed before and are assigned, based on energy arguments, to satellite Auger transitions from the O $1s^{-1}\,1\pi_u^{-1}\,1\pi_g^{+1}$

configuration to the configuration $1\pi_u^{-2}$. In detail, Sambe and Ramaker [60] assigned the Auger transition at 504.4 eV to O $1s^{-1}$ $1\pi_u^{-1}$ $1\pi_g^{+1}$ ($^2\Sigma^-$) → $1\pi_u^{-2}$ ($^3\Delta_u$) and the transition at 506.4 eV to O $1s^{-1}$ $1\pi_u^{-1}$ $1\pi_g^{+1}$ ($^4\Sigma^-$) → $1\pi_u^{-2}$ ($^3\Delta_u$). On the other hand, Larson et al. [33] assigned these transitions to O $1s^{-1}$ $1\pi_u^{-1}$ $1\pi_g^{+1}$ ($^2\Sigma^-$) → $1\pi_u^{-2}$ ($^3\Sigma_g^-$) and O $1s^{-1}$ $1\pi_u^{-1}$ $1\pi_g^{+1}$ ($^4\Sigma^-$) → $1\pi_u^{-2}$ ($^3\Sigma_g^-$), respectively. In the present partial Auger spectra presented in Fig. 4b) and c) the transition at 504.4 eV is clearly missing, while the transition at 506.4 eV is beyond the energy range studied in the present work. The absence of the first transition in Fig. 4b) and c) clearly supports the previous assignments to satellite Auger decays; an alternative assignment of this transition to O $1s^{-1}$ ($^2\Sigma^-$) → $1\pi_u^{-1}$ $1\pi_g^{-1}$ ($^3\Sigma_u^+$) can be completely excluded. The latter assignment can be considered rather unlikely - even without partial Auger spectra - because of a calculated zero intensity [24] as well as energy position arguments using the values obtained with different methods such as double charge transfer spectroscopy [55]. Energy position arguments are, however, not very strict since vibrational progressions can influence the peak position (see e.g. Fig. 7 and corresponding discussion).

According to Larson et al. there are three states that belong to the O $1s^{-1}$ $1\pi_u^{-1}$ $1\pi_g^{+1}$ configuration. These can be found 7.5 eV ($^2\Sigma^-$), 9.1 eV ($^4\Sigma^-$), and 11.4 eV ($^2\Sigma^-$) above the ionization threshold of the O $1s^{-1}$ ($^2\Sigma^-$) core-hole state [61]. Furthermore, they have an approximate relative intensity ratio of 0.8 : 1 : 0.1, respectively [61], so that the strongest satellite Auger transitions are expected to originate from the first two states. The calculations by Bao et al. [24] confirm that all other final states except $1\pi_u^{-2}$ ($^3\Delta_u$) and $1\pi_u^{-2}$ ($^3\Sigma_g^-$) can be excluded because of the expected energy positions. Using the energy positions derived in the present fit analysis (see Table 1) and the energy splitting of the satellite core-hole states relative to the O $1s^{-1}$ ($^2\Sigma^-$) core-hole state we derived the expected energy positions of 505.1 eV, 506.7 eV, 504.0 eV, and 505.6 eV for the transitions O $1s^{-1}$ $1\pi_u^{-1}$ $1\pi_g^{+1}$ ($^2\Sigma^-$) → $1\pi_u^{-2}$ ($^3\Delta_u$), O $1s^{-1}$ $1\pi_u^{-1}$ $1\pi_g^{+1}$ ($^4\Sigma^-$) → $1\pi_u^{-2}$ ($^3\Delta_u$), O $1s^{-1}$ $1\pi_u^{-1}$ $1\pi_g^{+1}$ ($^2\Sigma^-$) → $1\pi_u^{-2}$ ($^3\Sigma_g^-$) and O $1s^{-1}$ $1\pi_u^{-1}$ $1\pi_g^{+1}$ ($^4\Sigma^-$) → $1\pi_u^{-2}$ ($^3\Sigma_g^-$), respectively. Since a splitting of 2.0 eV between the two satellite Auger transitions under discussion clearly indicates that one final state is populated by the two satellite core-hole states O $1s^{-1}$ $1\pi_u^{-1}$ $1\pi_g^{+1}$ ($^2\Sigma^-$) and O $1s^{-1}$ $1\pi_u^{-1}$ $1\pi_g^{+1}$ ($^4\Sigma^-$), the present results do not favor one of the two possible assignments of the final states. Note that the differences between the expected and the real energy positions of the satellite Auger lines can be readily explained with the influence of the vibrational progression on the peak position, as already shown.

In summary, the assignment of the satellite Auger transitions is still unclear despite our considerably improved understanding of the Auger spectrum of O_2 since the work of Sambe and Ramaker [60] as well as of Larson et al. [33] was performed. Specific additional studies on this topic seem to be the most promising way to achieve a conclusive assignment of the satellite transitions under discussion.

IV. Summary

In this study, we have presented first data recorded with a new apparatus for electron, electron coincidence spectroscopy with high energy resolution at kinetic energies of several hundred eV. As an example, we have presented Auger spectra of the O_2 molecule, separated into contributions of the O $1s^{-1}$ ($^2\Sigma^-$) and O $1s^{-1}$ ($^4\Sigma^-$) core-hole states. In our data analysis we have combined these data with a newly recorded, conventional (non-coincident) Auger spectrum with excellent signal-to-noise ratio. Combining the advantages of these two methods with a state-of-the-art fit analysis has allowed an improved understanding of the Auger spectrum to be obtained. Our work is generally in line with the earlier experimental and theoretical published results on the Auger decay of O_2. In particular, we performed a Franck-Condon analysis of the Auger transitions to the dicationic final states W $^3\Delta_u$, B $^3\Pi_g$, and B' $^3\Sigma_u^-$ by using vibrational energies and anharmonicities reported in the literature. In this way we were able to obtain the equilibrium distances for these dicationic states. Finally our analysis shows that vibrational progressions are present in the spectrum but they are

masked by other effects such as the *gerade/ungerade* splitting of the O $1s^{-1}$ ($^4\Sigma^-$) core-hole state. From these results we conclude that photoelectron-Auger electron coincidence measurements recorded at a total resolution consisting of the analyzer resolution and the photon energy resolution of less than 100 meV should clearly display vibrational levels in the Auger spectrum. Such future spectra should allow the potential energy curves of the dicationic final states as well as the *gerade/ungerade* splitting of the O $1s^{-1}$ ($^4\Sigma^-$) core-hole state to be determined with high accuracy.

More generally, the present results highlight the potential of our electron-electron coincidence technique in terms of energy resolution and acquisition efficiency. Moreover, the use of the ArTOF results (typically) in an improved solid angle acceptance for the photoelectron compared to the TOF analyzers in our earlier set-up [17]. With the measurement presented here we have focused on obtaining an overview of the spin-state resolved Auger spectra. It was therefore not necessary to impose strict limits on the energy resolution. Potentially however the ArTOF is capable of an energy resolution at least in the few-meV range [21]. Although the energy resolution in a coincidence experiment will be slightly worse than the non-coincident values indicated in the above reference due to our multi-bunch timing scheme (see [17]), a substantial improvement over earlier experiments can be expected. First results demonstrating this will be published elsewhere [37].

Acknowledgements

R.P. gratefully acknowledges financial support by the Deutsche Forschungsgemeinschaft, project PU 180-6/1. Support from the BESSY II staff during performing the experiments is gratefully acknowledged.

Table 1: Results of the fit analysis in the kinetic energy region from 487.5 eV to 502 eV. Given are the kinetic energies, E_{kin}, the labeling, as well as the assignment of the transitions together with the configurations. For the configurations only changes in the occupancy of the orbitals relative to the ground state are indicated. In the region from 498 eV to 502 eV the energy positions of the v'' = 0 → v' = 0 are given while in the range from 487.5 eV to 498 eV the values refer to the peak positions. The labeling is adopted from Bao et al. [24] using numbers from 1 to 10. Figures indicated with prime denote Auger transitions originating from the O $1s^{-1}$ ($^2\Sigma^-$) core level and numbers without primes transitions originating from the O $1s^{-1}$ ($^4\Sigma^-$) core level. Note that the error bars for the kinetic energies do not include an error of 0.065 eV for the calibration of the entire energy scale.

E_{kin} (eV)	Labeling	Transition
501.83(1)	W (1')	O $1s^{-1}$ ($^2\Sigma^-$) → $1\pi_u^{-1}$ $1\pi_g^{-1}$ ($^3\Delta_u$)
500.88(1)	B (2')	O $1s^{-1}$ ($^2\Sigma^-$) → $3\sigma_g^{-1}$ $1\pi_g^{-1}$ ($^3\Pi_g$)
500.81(1)	W (1)	O $1s^{-1}$ ($^4\Sigma_u^-$) → $1\pi_u^{-1}$ $1\pi_g^{-1}$ ($^3\Delta_u$)
500.76(1)	W (1)	O $1s^{-1}$ ($^4\Sigma_g^-$) → $1\pi_u^{-1}$ $1\pi_g^{-1}$ ($^3\Delta_u$)
500.69(1)	B' (3')	O $1s^{-1}$ ($^2\Sigma^-$) → $1\pi_u^{-1}$ $1\pi_g^{-1}$ ($^3\Sigma_u^-$)
499.87(1)	B (2)	O $1s^{-1}$ ($^4\Sigma_u^-$) → $3\sigma_g^{-1}$ $1\pi_g^{-1}$ ($^3\Pi_g$)
499.82(1)	B (2)	O $1s^{-1}$ ($^4\Sigma_g^-$) → $3\sigma_g^{-1}$ $1\pi_g^{-1}$ ($^3\Pi_g$)
499.68(1)	B' (3)	O $1s^{-1}$ ($^4\Sigma_u^-$) → $1\pi_u^{-1}$ $1\pi_g^{-1}$ ($^3\Sigma_u^-$)
499.63(1)	B' (3)	O $1s^{-1}$ ($^4\Sigma_g^-$) → $1\pi_u^{-1}$ $1\pi_g^{-1}$ ($^3\Sigma_u^-$)
497.59(3)	4'	O $1s^{-1}$ ($^2\Sigma^-$) → $1\pi_u^{-2}$ ($^3\Delta_g$)
496.46(3)	4	O $1s^{-1}$ ($^4\Sigma^-$) → $1\pi_u^{-2}$ ($^3\Delta_g$)
	5'	O $1s^{-1}$ ($^2\Sigma^-$) → $3\sigma_g^{-1}$ $1\pi_u^{-1}$ ($^3\Pi_u$)
	7'	O $1s^{-1}$ ($^2\Sigma^-$) → $1\pi_u^{-2}$ ($^3\Sigma_g^-$)
495.93(3)	6'	O $1s^{-1}$ ($^2\Sigma^-$) → $3\sigma_g^{-1}$ $1\pi_u^{-1}$ ($^3\Pi_u$)
495.08(3)	5	O $1s^{-1}$ ($^4\Sigma^-$) → $3\sigma_g^{-1}$ $1\pi_u^{-1}$ ($^3\Pi_u$)
	7	O $1s^{-1}$ ($^4\Sigma^-$) → $1\pi_u^{-2}$ ($^3\Sigma_g^-$)
494.73(3)	6	O $1s^{-1}$ ($^4\Sigma^-$) → $3\sigma_g^{-1}$ $1\pi_u^{-1}$ ($^3\Pi_u$)
493.83(3)	a	
493.17(3)	8'	O $1s^{-1}$ ($^2\Sigma^-$) → $3\sigma_g^{-1}$ $1\pi_u^{-1}$ ($^3\Pi_u$)
492.63(3)	9'	O $1s^{-1}$ ($^2\Sigma^-$) → $1\pi_u^{-2}$ ($^3\Sigma_g^-$)
	10'	O $1s^{-1}$ ($^2\Sigma^-$) → $3\sigma_g^{-2}$ ($^3\Sigma_g^-$)
492.09(3)	8	O $1s^{-1}$ ($^4\Sigma^-$) → $3\sigma_g^{-1}$ $1\pi_u^{-1}$ ($^3\Pi_u$)
491.87(3)	9	O $1s^{-1}$ ($^4\Sigma^-$) → $1\pi_u^{-2}$ ($^3\Sigma_g^-$)
	10	O $1s^{-1}$ ($^4\Sigma^-$) → $3\sigma_g^{-2}$ ($^3\Sigma_g^-$)
490.57(3)	b	
489.65(3)	c	
489.14(3)	d	

References

[1] H.W. Haak, G.A. Sawatzky, T.D. Thomas, Phys. Rev. Lett. 41 (1978) 1825.
[2] E. Jensen, R.A. Bartynski, S.L. Hulbert, E.D. Johnson, R. Garrett, Phys. Rev. Lett. 62 (1989) 71.
[3] E. Jensen, R.A. Bartynski, S.L. Hulbert, E.D. Johnson, Rev. Sci. Instrum. 63 (1992) 3013.
[4] W.S.M. Werner, W. Smekal, H. Störi, H. Winter, G. Stefani, A. Ruocco, F. Offi, R. Gotter, A. Morgante, F. Tommasini, Phys. Rev. Lett. 94 (2005) 038302.
[5] M.Neeb, J.E. Rubensson, M. Biermann, W. Eberhardt, J. Phys. B, At. Mol. Opt. Phys. 29 (1996) 4381.
[6] J. Viefhaus, G. Snell, R. Hentges, M. Wiedenhöft, F. Heiser, O. Gessner, U. Becker, Phys. Rev. Lett. 80 (1998) 1618.
[7] P. Lablanquie, L. Andric, J. Palaudoux, U. Becker, M. Braune, J. Viefhaus, J.H.D. Eland, F. Penent, J. Electron Spectrosc. Relat. Phenom. 156-158 (2007) 51.
[8] V. Ulrich, S. Barth, S. Joshi, T. Lischke, A.M. Bradshaw, U. Hergenhahn, Phys. Rev. Lett. 100 (2008) 143003.
[9] S. Rioual, B. Rouvellou, L. Avaldi, G. Battera, R. Camilloni, G. Stefani, G. Turri, Phys. Rev. Lett. 86 (2001) 1470.
[10] S. Rioual, B. Rouvellou, A. Huetz, L. Avaldi, Phys. Rev. Lett. 91 (2003) 173001.
[11] P. Bolognesi, A. De Fanis, M. Coreno, L. Avaldi, Phys. Rev. A 70 (2004) 022701.
[12] P. Bolognesi, M. Coreno, L. Avaldi, L. Storchi, F. Tarantelli, J. Chem. Phys. 125 (2006) 54306.
[13] P. Bolognesi, R. Püttner, L. Avaldi, Chem. Phys. Lett. 464 (2008) 21.
[14] P. Bolognesi, P. O'Keeffe, L. Avaldi, J. Phys. Chem. A 113 (2009) 15136.
[15] P. Bolognesi, A. Kivimäki, P. O'Keeffe, V. Feyer, F. Tarantelli, L. Storchi, L. Avaldi, J. Chem. Phys. 134 (2011) 094308.
[16] P. Bolognesi, D.B. Thompson, L. Avaldi, M.A. MacDonald, M.C.A. Lopes, D.R. Cooper, G.C. King, Phys. Rev. Lett. 82 (1999) 2075.
[17] V. Ulrich, S. Barth, T. Lischke, S. Joshi, T. Arion, M. Mucke, M. Förstel, A.M. Bradshaw, U. Hergenhahn, J. Electron Spectrosc. Relat. Phenom. 183 (2011) 70.
[18] D. Schröder, H. Schwarz, J. Phys. Chem. A 103 (1999) 7385.
[19] R. Püttner, X.-J. Liu, H. Fukuzawa, T. Tanaka, M. Hoshino, H. Tanaka, J. Harries, Y. Tamenori, V. Carravetta, K. Ueda, Chem. Phys. Lett. 445 (2007) 6.
[20] R. Püttner, T. Arion, M. Förstel, T. Lischke, M. Mucke, V. Sekushin, G. Kaindl, A.M. Bradshaw, U. Hergenhahn, Phys. Rev. A 83 (2011) 043404.
[21] G. Öhrwall, P. Karlsson, M. Wirde, M. Lundqvist, P. Andersson, D. Ceolin, B. Wannberg, T. Kachel, H. Dürr, W. Eberhardt, S. Svensson, J. Electron Spectrosc. Relat. Phenom. 183 (2011) 125.
[22] W.S.M. Werner, A. Ruocco, F. Offi, S. Iacobucci, W. Smekal, H. Winter, G. Stefani, Phys. Rev. B 78 (2008) 233403.
[23] F.O. Schumann, C. Winkler, J. Kirschner, Phys. Rev. Lett. 98 (2007) 257604.
[24] Z. Bao, R.F. Fink, O. Travnikova, D. Céolin, S. Svensson, M.N. Piancastelli, J. Phys. B 41 (2008) 125101.
[25] S. L. Sorensen, K.J. Borve, R. Feifel, A. de Fanis, K. Ueda, J. Phys. B 41 (2008) 095101.
[26] U. Hergenhahn, J. Phys. B 37 (2004) R89.
[27] U. Hergenhahn, O. Kugeler, A. Rüdel, E.E. Rennie, A.M. Bradshaw, J. Phys. Chem. A 105 (2001) 5704.
[28] B. Kempgens, H. Köppel, A. Kivimäki, M. Neeb, L.S. Cederbaum, A.M. Bradshaw, Phys. Rev. Lett. 79 (1997) 3617.

[29] K.J. Børve, L.J. Sæthre, T.D. Thomas, T.X. Carroll, N. Berrah, J.D. Bozek, E. Kukk, Phys. Rev. A 63 (2001) 012506.
[30] N. Kosugi, Chem. Phys. 289 (2003) 117.
[31] K. Siegbahn, ESCA applied to free molecules, North-Holland, Amsterdam, 1969.
[32] W. E. Moddeman, T. A. Carlson, M. O. Krause, B. P. Pullen, W. E. Bull, and G. K. Schweitzer, J. Chem. Phys. 55 (1971) 2317.
[33] M. Larson, P. Baltzer, S. Svensson, B. Wannberg, N. Mårtensson, A. Naves de Brito, N. Correia, M.P. Keane, M. Carlsson-Göthe, L. Karlsson, J. Phys. B 23 (1990) 1175.
[34] J.H.D. Eland, Chem. Phys. 294 (2003) 171.
[35] R. Feifel, J.H.D. Eland, D. Edvardsson, J. Chem. Phys. 122 (2005) 144308.
[36] G. Dawber, A.G. McConkey, L. Avaldi, M.A. MacDonald, G.C. King, R.I. Hall, J. Phys. B 27 (1994) 2191.
[37] C. Lupulescu, T. Arion, R. Ovsyannikov, R. Püttner, G. Gavrila, S. Svensson, A.M. Bradshaw, U. Hergenhahn, W. Eberhardt, to be published.
[38] P. D. C. King, R. C. Hatch, M. Bianchi, R. Ovsyannikov, C. Lupulescu, G. Landolt, B. Slomski, J. H. Dil, D. Guan, J. L. Mi, E. D. L. Rienks, J. Fink, A. Lindblad, S. Svensson, S. Bao, G. Balakrishnan, B. B. Iversen, J. Osterwalder, W. Eberhardt, F. Baumberger, Ph. Hofmann, Phys. Rev. Lett. 107 (2011) 096802.
[39] Y. H. Wang, D. Hsieh, D. Pilon, L. Fu, D. R. Gardner, Y. S. Lee, N. Gedik, Phys. Rev. Lett. 107 (2011) 207602.
[40] A. Vollmer, R. Ovsyannikov, M. Gorgoi, S. Krause, M. Oehzelt, A. Lindblad, N. Mårtensson, S. Svensson, P. Karlsson, M. Lundqvuist, T. Schmeiler, J. Pflaum, N. Koch, J. Electron Spectrosc. Relat. Phenom. 185 (2012) 55.
[41] M. Ogawa, S. Yamamoto, Y. Kousa, F. Nakamura, R. Yukawa, A. Fukushima, A. Harasawa, H. Kondoh, Y. Tanaka, A. Kakizaki, I. Matsuda, Rev. Sci. Instrum. 83 (2012) 023109.
[42] O. Hemmers, S. B. Whitfield, P. Glans, H. Wang, D. W. Lindle, R. Wehlitz, I. A. Sellin, Rev. Sci. Instrum. 69 (1998) 3809.
[43] M. Abo-Bakr, W. Anders, P. Kuske, G. Wüstefeld, in: P.L. Joe Chew, S. Webber (Eds.), Particle Accelerator Conference, Vol. Catalog Number 03CH37423C, IEEE, Portland, OR, 2003, p. 3020.
[44] O. Kugeler, S. Marburger, U. Hergenhahn, Rev. Sci. Instrum. 74 (2003) 3955.
[45] O. Kugeler, Ph.D. Thesis, Technische Universität Berlin, 2003, http://opus.kobv.de/tuberlin/volltexte/2004/693/.
[46] B. Wannberg, Nucl. Instrum. and Meth. A, 601, (2009) 182.

[47] T. Gießel, D. Bröcker, P. Schmidt, W. Widdra, Rev. Sci. Instrum. 74 (2003) 4620.
[48] M. Lundqvist, D. Edvardsson, P. Baltzer, M. Larson and B. Wannberg, J. Phys. B 29 (1996) 499.
[49] S. Sorensen, T. Tanaka, R. Feifel, J. H. D. Eland, M. Kitajima, H. Tanaka, R. Sankari, A. De Fanis, M. N. Piancastelli, L. Karlsson, K. Ueda, Chem. Phys. Lett. 398 (2004) 168.

[50] B. X. Yang, D. M. Manson, and K. Tohji, J. Chem. Phys. 89 (1988) 1215.
[51] M. Mahalingam and D. M. Hanson, J. Chem. Phys. 97(1992) 2183.
[52] B. Krässig, M. Jung, D. Gemmell, E. Kanter, T. LeBrun, S. Southworth, and L. Young, Physical Review Letters 75 (1995) 4736.
[53] N.A. Cherepkov, S.K. Semenov, and R. Dörner, Journal of physics: Conference Series 141 (2008) 012001.
[54] K. Hosaka, J. Adachi, A. Golovin, M. Takahashi, T. Teramoto, N. Watanabe, T. Jahnke, T. Weber, M. Schöffler, L. Schmidt, T. Osipov, O. Jagutzki, A. Landers, M. Prior, H.

Schmidt-Böcking, R. Dörner, A. Yagishita, S. Semenov, and N. Cherepkov, Phys. Rev. A 73 (2006) 022716.
[55] O. Furuhashi, T. Kinugawa, T. Hirayama, T. Koizumi, C. Yamada and S. Ohtani, Phys. Rev. A 70 (2004) 052501.
[56] R. Püttner, H. Fukuzawa, X.-J. Liu, S. K. Semenov, N. A. Cherepkov, T. Tanaka, M. Hoshino, H. Tanaka and K. Ueda, J. Phys. B 41 (2008) 141001.
[57] R. Püttner, Y. F. Hu, G. M. Bancroft, H. Aksela, E. Nõmmiste, J. Karvonen, A. Kivimäki, S. Aksela, Phys. Rev. A 59 (1999) 4438.
[58] K. P. Huber, G. Herzberg, Molecular Spectra and Molecular Structure Vol. IV: Constants of Diatomic Molecules, Van Nostrand Reinhold, New York, 1979.
[59] G. B. Armen, J. Tulkki, T. Åberg, and B. Crasemann, Phys. Rev. A 36 (1987) 5606.
[60] H. Sambe and D. E. Ramaker, Chem. Phys. 104, 331 (1986).
[61] D. Nordfors, A. Nilsson, N. Mårtensson, S. Svensson, and U. Gelius, Institute of Physics Report UUIP-1206, Uppsala University, 1989.

Figure captions

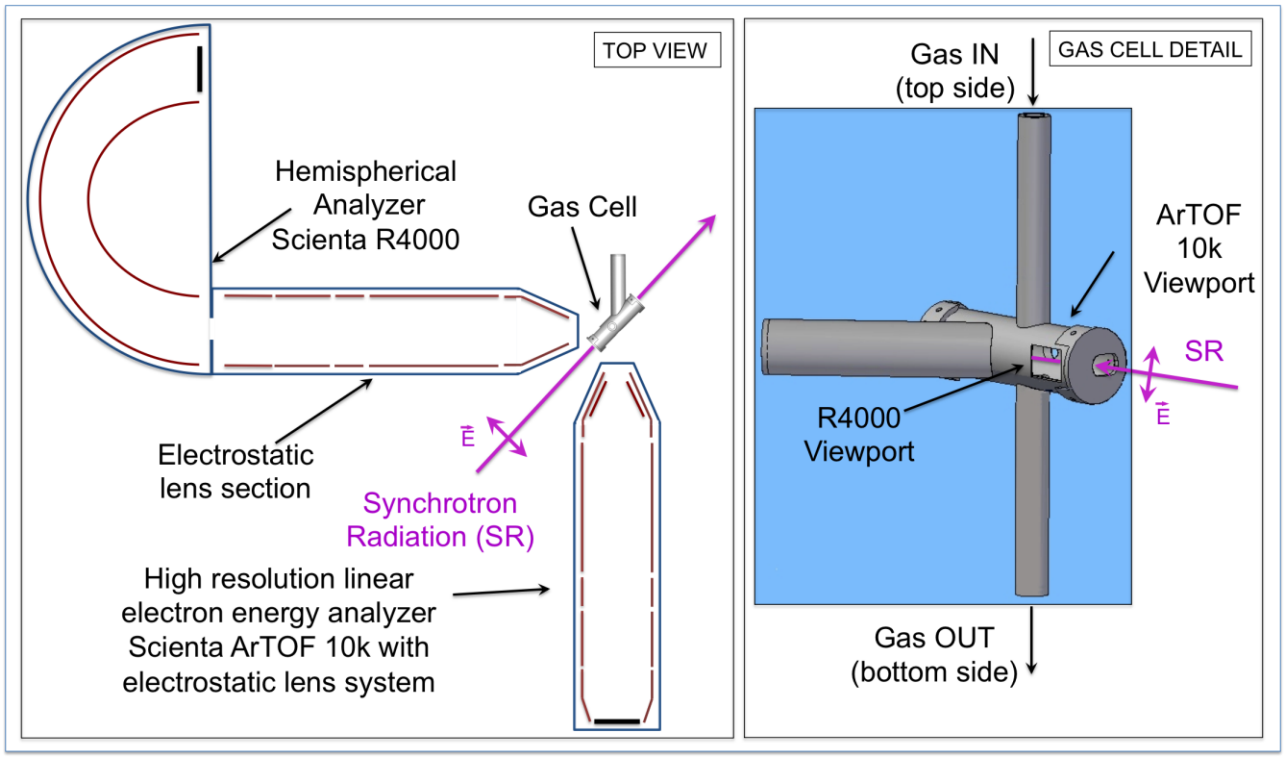

Fig. 1. Schematics of the experimental setup, showing the two high-resolution electron energy analyzers oriented 90° to each other, and 45° to the direction of the synchrotron radiation. In the inset, we show an enlarged sketch of the constructed gas cell, used for gaseous samples (see text for more details).

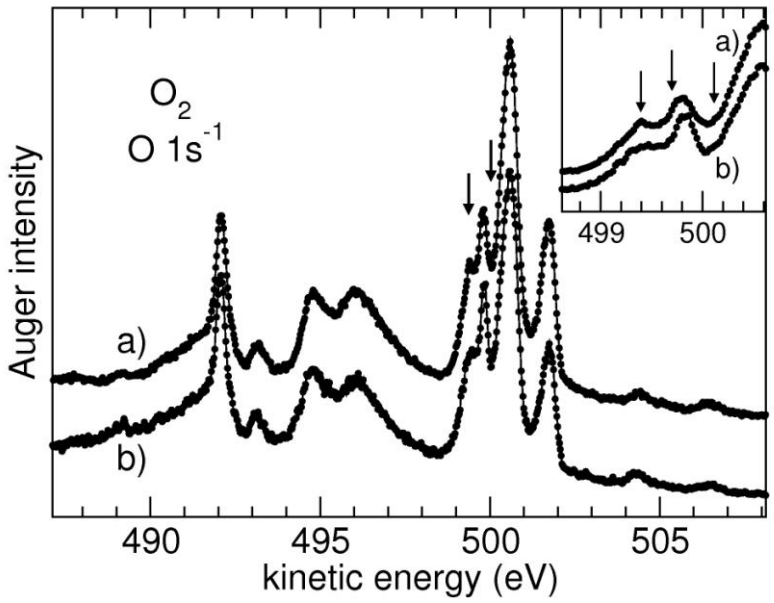

Fig. 2. a) High resolution Auger spectrum of O_2, obtained after ionization with hν = 573.1 eV photons. The spectrum was recorded by using the hemispherical spectrometer of our set-up in the conventional, non-coincident (swept) mode, and with the standard CCD detector. A pass energy of 100 eV and analyzer slit settings of 200 μm allowed for an analyzer energy resolution of 50 meV. b) Another high resolution spectrum measured at SPring8 with hν = 650 eV and a comparable energy resolution [49]. The vertical arrows around 499 eV indicate differences between the two spectra in this energy region. For better comparison the inset shows the two spectra in the energy region from 498.5 eV to 500.5 eV. The three vertical arrows indicate energy positions where differences were observed during the fit analysis; for details, see text.

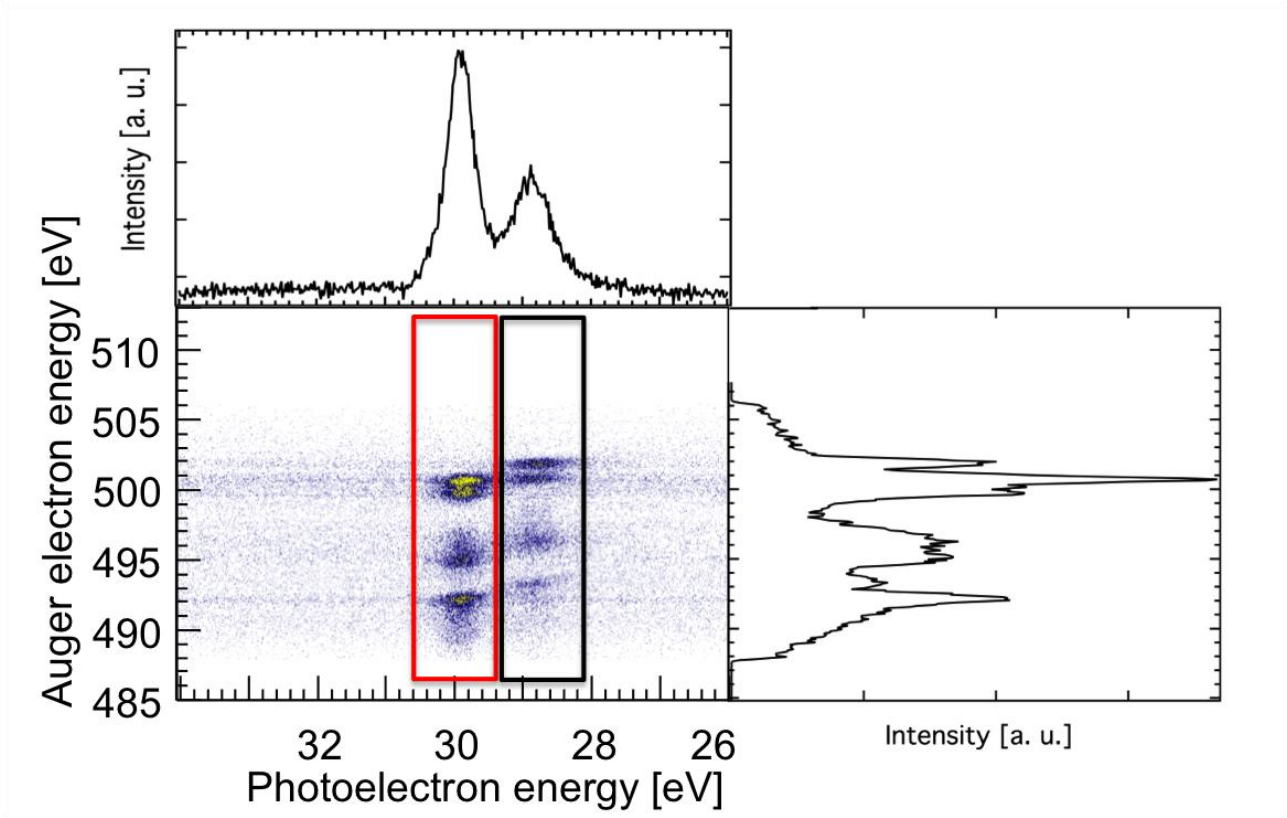

Fig. 3. (Color online) Center panel: photoelectron-Auger electron coincidence spectrum of O_2 recorded at hν = 573.1 eV, as a color-coded map. Upper and right panel, respectively: photoelectron (Auger electron energy) spectrum, as obtained by summing up the coincidence map along the vertical (horizontal) axis of the spectrum. The red and black rectangles indicate the regions of the coincidence map used for obtaining the Auger electron energy spectra pertaining to the individual intermediate states of the cation (see text for details).

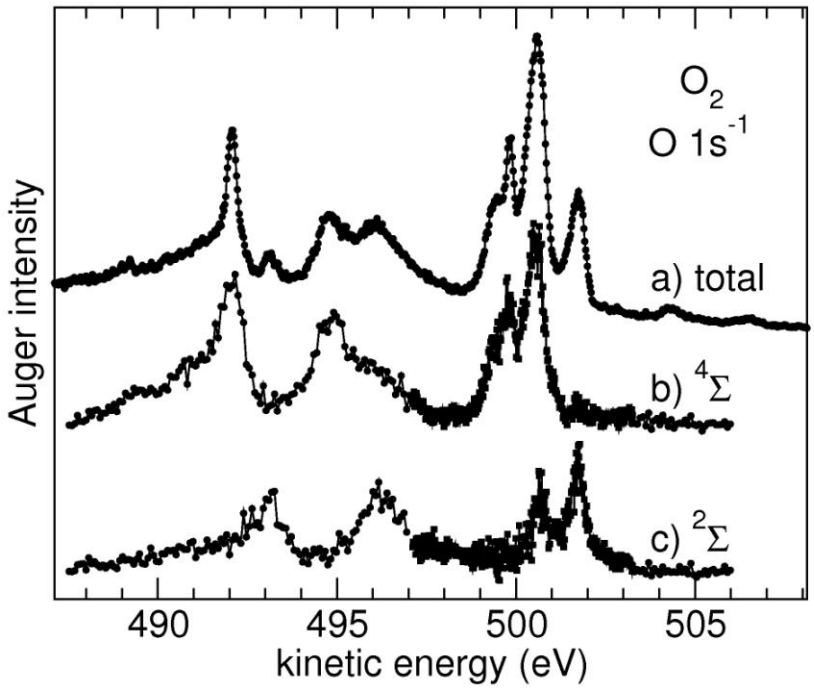

Fig. 4: Total normal Auger spectrum (a) as well as Auger spectra originating from the $^4\Sigma^-$ (b) and $^2\Sigma^-$ (c) core-hole states in the energy range from 487 eV to 508 eV. The latter two spectra are derived from coincidence measurements, and have been assembled from data of this work (Fig. 3, energy range below 497 eV and above 503 eV), and an earlier data set which had covered only the range from 497 eV to 503 eV [17] (see text for details).

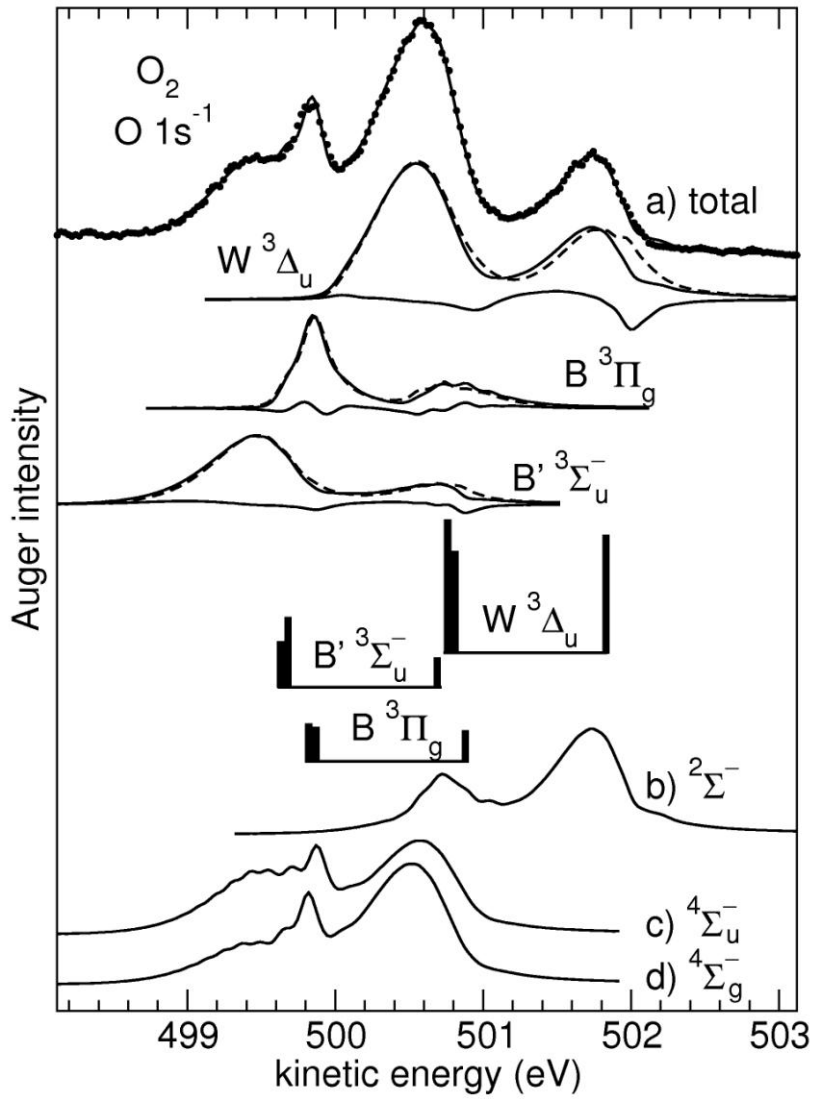

Fig. 5. The Auger spectrum in the energy range from 497 eV to 503 eV in detail. (a) The total non-coincident Auger spectrum [49]. The solid line through the data points represents the fit result. The vertical bar diagrams indicate the relative intensities and the v'' = 0 → v' = 0 energy positions for the Auger transitions from the core-hole states O $1s^{-1}$ ($^4\Sigma^-_g$), O $1s^{-1}$ ($^4\Sigma^-_u$), and O $1s^{-1}$ ($^2\Sigma^-$) to the dicationic final states W $^3\Delta_u$, B $^3\Pi_g$, and B' $^3\Sigma^-_u$, and the sub-spectra display the spectral contributions of these Auger transitions. For each Auger transition to the individual final states the upper (lower) solid sub-spectrum displays the entire vibrational progression (the vibrational lifetime interference contributions). The dashed sub-spectra indicate the vibrational progression without lifetime interference contributions. The traces designated as (b), (c), and (d) display the contributions of the spectrum which originate according to the fit analysis from the $^2\Sigma^-$, $^4\Sigma^-_u$ and the $^4\Sigma^-_g$ core holes, respectively.

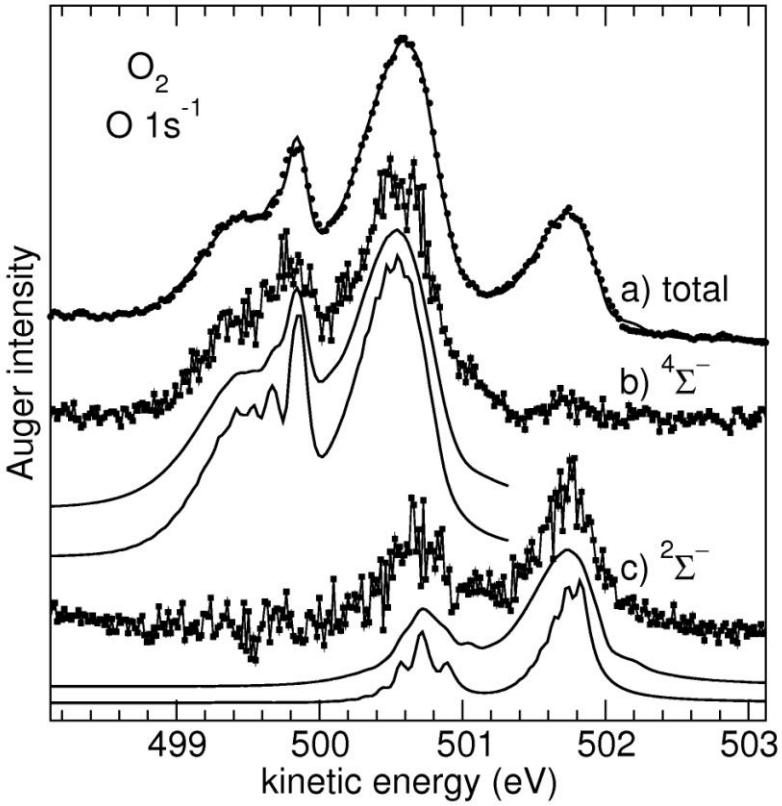

Fig. 6. The Auger spectrum in the energy range from 497 eV to 503 eV in detail. (a) The total conventional Auger spectrum [49]. The solid line through the data points represents the fit result. (b) and (c) display the contributions of the spectrum which originate from the $^4\Sigma^-$ and the $^2\Sigma^-$ core holes, respectively. For (b) and (c) the upper sub-spectrum displays the corresponding spectrum based on the fit result shown in (a). The lower solid line sub-spectra indicate a simulation of the Auger spectra originating from the v'' = 0 level of the core ionized state by assuming a total width (energy resolution plus lifetime broadening) of 100 meV. For more details, see text.

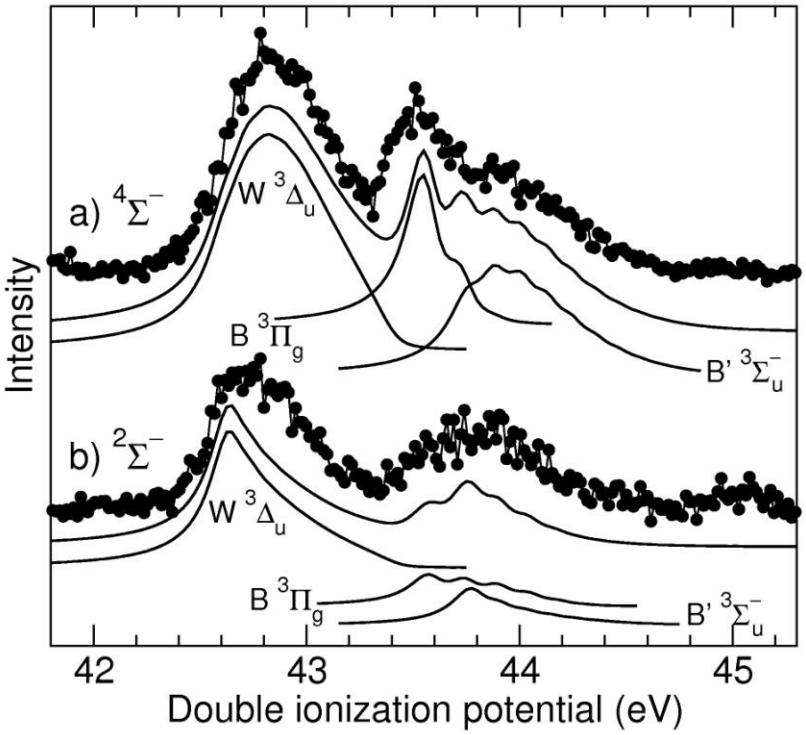

Fig. 7: Final-state energy spectra obtained from the same coincidence measurements as used for the spectra presented in Fig. 6. The spectra displayed in a) and b) show the final-state energy spectra obtained via a population through the $^4\Sigma^-$ and the $^2\Sigma^-$ core holes. In each case, the upper solid line sub-spectrum shows a simulation based on the present fit results and the three lower sub-spectra the contributions of the individual Auger transitions.

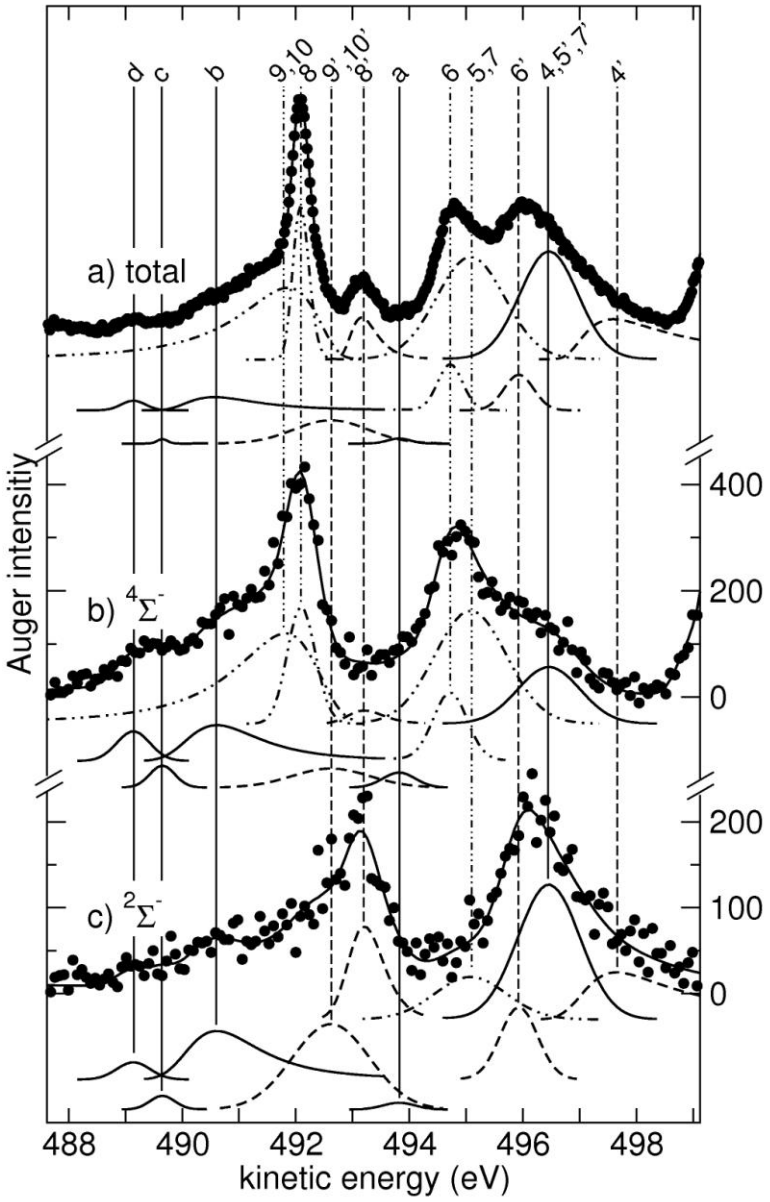

Fig. 8. The total conventional Auger spectrum measured in the present work (a) as well as the $^4\Sigma^-$ (b) and the $^2\Sigma^-$ (c) spectra in the kinetic-energy region from 487.6 eV to 499.1 eV. For comparison, intensities for the $^4\Sigma^-$ and the $^2\Sigma^-$ spectrum are given on the right side of the figure. The solid lines through the data points represent the fit results. The sub-spectra indicate the fit result obtained using asymmetric Gaussian lines. Their energy positions are indicated by vertical lines. Solid-line sub-spectra and vertical lines indicate peaks, which are present in both, the $^4\Sigma^-$ and the $^2\Sigma^-$ spectrum. Contrary to this the dashed and dash-dotted lines and sub-spectra represent peaks which are predominantly or solely visible in the $^4\Sigma^-$ and the $^2\Sigma^-$ spectrum, respectively. Peaks with vanishing intensity in one of the partial spectra are not indicated in this spectrum. For details on labeling the peaks, see text.